

## Bayesian Analysis for Remote Biosignature Identification on exoEarths (BARBIE) IV: Analyzing CO<sub>2</sub> Detections in the Near-IR to Determine the Long-Wavelength Cut-off for the Habitable Worlds Observatory Coronagraph

CELESTE HAGEE,<sup>1,2,3</sup> NATASHA LATOUF,<sup>4,1,2,\*</sup> AVI M. MANDELL,<sup>1,2</sup> MICHAEL D. HIMES,<sup>5,1</sup> MICHAEL DANE MOORE,<sup>1,6,2</sup> AND GERONIMO L. VILLANUEVA<sup>1,2</sup>

<sup>1</sup>*NASA Goddard Space Flight Center, 8800 Greenbelt Road, Greenbelt, MD 20771, USA*

<sup>2</sup>*Sellers Exoplanets Environment Collaboration, 8800 Greenbelt Road, Greenbelt, MD 20771, USA*

<sup>3</sup>*Southeastern Universities Research Association, 1201 New York Ave. NW, Suite 430 Washington, DC 20005 USA*

<sup>4</sup>*Department of Physics and Astronomy, George Mason University, 4400 University Drive MS 3F3, Fairfax, VA 22030, USA*

<sup>5</sup>*Morgan State University, 1700 E Cold Spring Lane, Baltimore, MD 21251, USA*

<sup>6</sup>*Business Integra, Inc., Bethesda, MD, USA.*

### ABSTRACT

We present our analysis of how the detectability of carbon dioxide (CO<sub>2</sub>) on an Earth-like planet varies with respect to signal-to-noise ratio (SNR), wavelength, and molecular abundance. Using the Bayesian Analysis for Remote Biosignature Identification on exoEarths (BARBIE) methodology, we can inform the optimal long-wavelength cut-off for the future Habitable Worlds Observatory (HWO) coronagraph. We test 25 evenly-spaced 20% bandpasses between 0.8-2.0 $\mu$ m, and simulate data spanning a range of SNRs and molecular abundance to analyze the relationship between wavelength and detectability for different planetary archetypes. We examine abundance levels from varying Earth epochs and a Venus-like archetype to investigate how detectability would change throughout the evolution of a rocky planet. Here, we present our results on the planetary conditions and technological requirements to strongly detect CO<sub>2</sub>. In addition, we analyze the degeneracy of CO<sub>2</sub> with carbon monoxide (CO), methane (CH<sub>4</sub>), and water (H<sub>2</sub>O). We determine that any abundance of CO does not achieve strong detections and that CH<sub>4</sub> and H<sub>2</sub>O play a pivotal role in the ability to detect CO<sub>2</sub>. We conclude that the optimal long-wavelength cut-off for the Habitable Worlds Observatory coronagraph should be 1.68 $\mu$ m.

### 1. INTRODUCTION

Since the first discovery of an exoplanet around a main-sequence star in 1995 (Mayor & Queloz 1995), more than 6,000 exoplanets have been discovered (Akeson et al. 2013). Astronomers are now looking towards characterizing these exoplanets, especially small, terrestrial planets, to tell us more about their formation, evolution, and composition. However, in order to constrain the properties of potentially Earth-like exoplanets around Sun-like stars, future telescopes will need to use high-contrast direct imaging, which requires a highly effective starlight suppression system such as a high-contrast coronagraph or starshade (Roberge & Moustakas 2018; The LUVOIR Team 2019; Gaudi et al. 2020). Based on the recommendations of the National Academies of Sciences, Engineering, and Medicine (2021), NASA began developing a future space telescope that could accomplish this goal; this concept is now called the Habitable Worlds Observatory (HWO). HWO will be designed to have the technological imaging capability to detect and characterize Earth-like planets and identify signs of planetary habitability and possibly biology. Naturally, one of the key instruments currently in active development for HWO is the coronagraph instrument, nominally planned to have the capability to observe in  $\sim$ 20% bandpasses across the UV, visible, and NIR wavelength regimes (The LUVOIR Team 2019; Juanola-Parramon et al. 2022).

Corresponding author: Celeste Hagee  
 celeste.hagee@email.ucr.edu

\* NSF Graduate Research Fellow, 2415 Eisenhower Ave, Alexandria, VA 22314

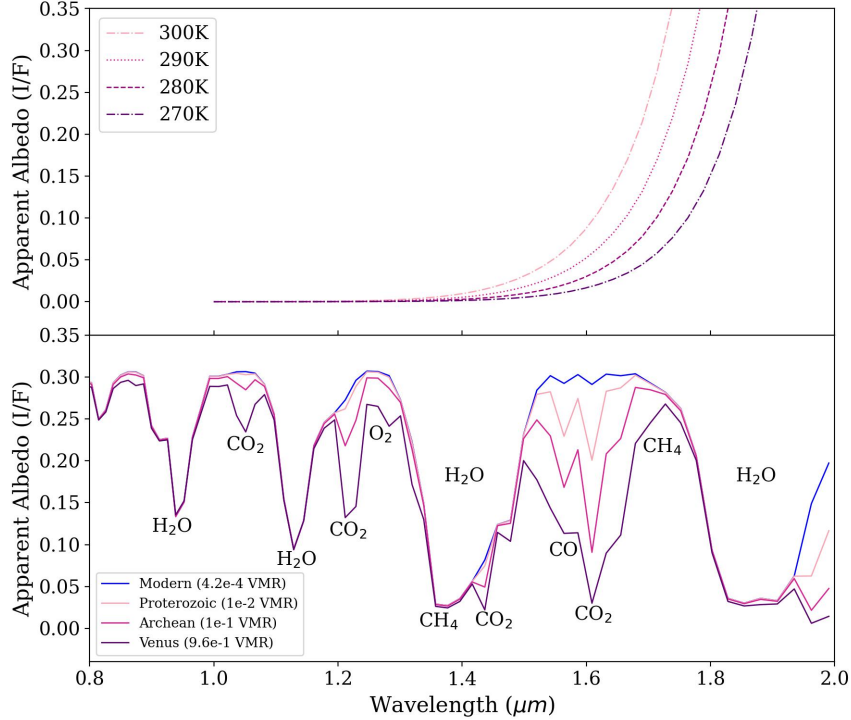
A yet-undetermined parameter for the coronagraph instrument is the long-wavelength cut-off. One of the driving factors for constraining the long-wavelength cut-off in the NIR is the telescope temperature. At higher telescope temperatures, a higher background flux will contribute to a higher overall photon noise, impacting the exposure time necessary to reach a required SNR. Two strategies can help avoid the impact of a higher thermal background on spectral characterization: targeting spectral features at shorter wavelengths, where absorption features are weaker but thermal background is minimal, or cooling the telescope to enable low-background noise measurements of deeper spectral features at longer wavelengths.

Figure 1 illustrates this trade-off. The top panel shows how noise from the blackbody emission of the telescope, henceforth called thermal noise, fluctuates with respect to four varying temperatures (270K in dark purple, 280K in purple, 290K in deep pink, and 300K in light pink). The bottom panel illustrates how spectral features are impacted by wavelength and molecular abundance by plotting four modern-Earth spectra with Modern, Proterozoic-like, Archean-like, and Venus-like  $\text{CO}_2$  abundances with labeled water ( $\text{H}_2\text{O}$ ), methane ( $\text{CH}_4$ ), oxygen ( $\text{O}_2$ ), carbon monoxide ( $\text{CO}$ ), and carbon dioxide ( $\text{CO}_2$ ) features over  $0.8\text{-}2.0\mu\text{m}$ .

It is clear that for wavelengths past  $\sim 1.3\mu\text{m}$ , higher telescope temperatures produce more noise. However, cooling a massive space telescope below room temperature ( $\sim 300\text{K}$ ) increases the overall cost dramatically, due to the need for fabrication and testing facilities operating at these temperatures. Additionally, cooling a telescope below room temperature has shown decreased stability in dynamic damping and mirror materials and would require abandoning the current coronagraph technology developments (Feinberg 2016). Cooling the telescope could be reevaluated in the future if advancements such as new cryogenic technologies are made. However, we move forward with this study based on the current baseline of having a telescope operating at room temperature. Thus, our goal is to determine whether exoplanet characterization is possible with a room temperature telescope (i.e., below  $1.7\mu\text{m}$ ). This will enable us to find the optimal long-wavelength cut-off that provides the opportunities to maximize our spectral characterization while minimizing additional costs.

At NIR wavelengths, many molecules of interest have absorption features, as shown in the bottom panel of Figure 1. In particular, we can visually see that  $\text{H}_2\text{O}$ ,  $\text{CH}_4$ , and  $\text{O}_2$  all have deep features at shorter NIR wavelengths, and thus are not the science drivers for the coronagraph long-wavelength cut-off. However,  $\text{CO}_2$  and  $\text{CO}$  have their most absorbent features at wavelengths longer than  $1.4\mu\text{m}$ , with relatively weak features (or no features) at shorter wavelengths. To illustrate this further,  $\text{CO}_2$  and  $\text{CO}$  spectra at three varying abundances each - instead of a full modern-Earth spectra - are plotted in Figure 2. It is evident that  $\text{CO}_2$  features are significantly deeper at longer wavelengths. The only apparent  $\text{CO}$  feature is at  $1.58\mu\text{m}$ , and even at the highest abundance -  $1\times 10^{-2}$  VMR - the absorption depth does not compare with  $\text{CO}_2$  features at the same wavelength. Thus, the main focus of this study is to determine the optimal bandpass that  $\text{CO}_2$  can be strongly detected to constrain the long-wavelength cut-off for the HWO coronagraph.

We used the established Bayesian Analysis for Remote Biosignature Identification on exoEarths (BARBIE) project methodology (Latouf et al. (2023, 2024, 2025), hereafter BARBIE1, BARBIE2, BARBIE3, respectively) to understand the detectability of  $\text{CO}_2$  and the molecules that could impact it such as  $\text{CO}$ ,  $\text{H}_2\text{O}$ , and  $\text{CH}_4$ . Following the BARBIE methodology, our goal is determine the optimal single bandpass across the full  $0.8\text{-}2.0\mu\text{m}$  spectral range that would provide the best opportunity to achieve a strong  $\text{CO}_2$  detection in a single observation. This would enable a solid detection even under the scenario where HWO only performs spectroscopy with a single coronagraphic bandpass. Under a scenario with multiple parallel coronagraphic channels, this enables us to identify which bandpasses can cover a wide range of molecules. Thus, each channel can be optimized to obtain spectral information from as many molecules in the exoplanet's atmosphere as possible. This research analyzes unknown Earth-like exoplanet atmosphere compositions by testing a wide range of  $\text{CO}_2$ ,  $\text{H}_2\text{O}$ , and  $\text{CH}_4$  abundances throughout the history of an Earth-like planet. Additionally, we get a deeper understanding of how overlapping  $\text{CO}_2$ ,  $\text{CO}$ ,  $\text{H}_2\text{O}$ , and  $\text{CH}_4$  spectral features impact each other and their detectability. Combined with previous BARBIE studies, which analyzed the detectability of  $\text{O}_2$ ,  $\text{O}_3$ ,  $\text{H}_2\text{O}$ , and  $\text{CH}_4$  at shorter wavelengths, we will be able to determine the optimal long-wavelength cut-off that ensures we achieve strong detections for all biosignatures of interest with minimal engineering complications at a reasonable cost for the HWO coronagraph. In Section 2, we provide an overview of our methodology, including descriptions of the KEN grids. In Section 3, we present our results from the simulations of  $\text{CO}_2$  on Earth-like and Venus-like planetary archetypes using two different grids: L-KEN and B-Ken. Furthermore, we discuss our analysis of  $\text{CO}_2\text{-H}_2\text{O}$  and  $\text{CO}_2\text{-CH}_4$  degeneracies and how our results inform the optimal HWO coronagraph long-wavelength cut-off. Lastly, we analyze how four planetary archetypes, with combinations of low and high abundances of  $\text{CH}_4$  and



**Figure 1.** Illustrates the balancing act of keeping thermal noise minimal while maximizing the detectability of spectral features like CO<sub>2</sub> and CO. The top plot shows the relative noise based on varying telescope temperature between 0.8-2.0  $\mu\text{m}$ . The bottom plot shows spectral features from 0.8-2.0  $\mu\text{m}$  of H<sub>2</sub>O, CH<sub>4</sub>, O<sub>2</sub>, CO, and CO<sub>2</sub>. We plot a modern-Earth spectra using the Planetary Spectrum Generator (PSG) with four varying CO<sub>2</sub> abundances: Modern ( $4.2 \times 10^{-4}$  VMR) in dark blue, Proterozoic-like ( $1 \times 10^{-2}$  VMR) in light pink, Archean-like ( $1 \times 10^{-1}$  VMR) in magenta, and Venus-like ( $9.6 \times 10^{-1}$  VMR) in purple. The figure plots wavelength ( $\mu\text{m}$ ) on the x-axis and apparent albedo (I/F) on the y-axis.

**Table 1.** Atmospheric parameters for a modern-Earth twin for our fiducial data spectrum following Feng et al. (2018)

Parameter	Value
H <sub>2</sub> O Isotropic VMR	$3 \times 10^{-3}$
CH <sub>4</sub> Isotropic VMR	$1.65 \times 10^{-6}$
CO <sub>2</sub> Isotropic VMR	$3.8 \times 10^{-4}$
Constant temperature profile	250K
Surface Albedo (A <sub>s</sub> )	0.3
Pressure (P <sub>0</sub> )	1 bar
Fixed planetary radius at R <sub>p</sub>	1 R <sub>⊕</sub>

H<sub>2</sub>O, would perform given our long-wavelength cut-off. In Section 4, we present our conclusions and discuss our next steps in the BARBIE world.

## 2. METHODOLOGY

### 2.1. BARBIE Methodology

We follow the same methodology as BARBIE1, BARBIE2 & BARBIE3 to analyze the detectability of CO<sub>2</sub> under different assumptions for abundance and wavelength. In this section, we summarize the main steps of our analysis. For additional information on the details of model grid development, validation, and spectral retrieval methodology, please refer to the previous BARBIE studies.

First, following Feng et al. (2018), we set a modern-Earth twin with an isotropic atmosphere for our fiducial data spectrum as seen in Table 1. We also compiled an array of literature-sourced abundances for CO<sub>2</sub> from various epochs of Earth's history (Mahieux et al. 2023; Kaltenegger et al. 2007; Consortium\*† et al. 2023; Dr. Xin Lan &

**Table 2.** Detection strength definitions

Criterion	Detection Strength
$\ln B < 2.5$	unconstrained
$2.5 \leq \ln B < 5$	weak
$\ln B \geq 5$	strong

Dr. Ralph Keeling 2025), as shown in Table 3, in order to simulate Earth’s spectrum at different snapshots of time, enabling the investigation of how detectability varies across a physically-motivated range of abundances. BARBIE is a 1D model that utilizes the Planetary Spectrum Generator (PSG) (PSG; Villanueva et al. 2018) for the spectral simulations. PSG is a publicly accessible radiative transfer modeling tool that generates synthetic planetary spectral data across UV to Radio wavelengths for various target and observation assumptions. Molecular opacities are obtained from PSG which utilizes HITRAN (Gordon et al. 2022). The spectra are simulated with an atmosphere that is 50% cloudy and 50% clear.

The PSG framework for target and observatory parameterization has also been used for the related Bayesian inference tool called PSGnest<sup>1</sup>. PSGnest utilizes a custom implementation of the MultiNest nested sampling routine to enable Bayesian nested sampling retrievals using pre-computed grids of PSG-derived spectra. The PSGnest results produce several outputs: the maximum-likelihood values, the averages from the posterior distributions, uncertainties, and log-evidence (logZ) (Villanueva et al. 2018). For each retrieval, we calculate the log-Bayes factor ( $\ln B$ ; Benneke & Seager 2013) by subtracting the Bayesian log-evidence for a retrieval without the molecule from the Bayesian log-evidence for a retrieval with the molecule. Thus,  $\ln B$  directly compares fits by examining if an improved fit occurs with the molecule included, and addresses the likelihood of the presence of the molecular species and its detectability. We shift our definition of detection strength from the original Benneke & Seager (2013) as detailed in Table 2. If you are interested in the relationship between the log-Bayes Factor and the sigma value, please refer to Table 2 in Benneke & Seager (2013).

$\ln B$  directly investigates the presence or absence of the molecule in the atmosphere and calculates which scenario results in a better fit.  $\ln B$  is only calculated for gaseous components since those factors can be absent. We also calculate the upper limit, median value, and lower limit of the 68% credible region (Harrington et al. 2022). The 68% credible region includes the true value 68% of the time and informs us of the range of molecular abundances that are consistent with our data.

The abundance of CO<sub>2</sub> has drastically varied over the course of Earth’s history (Kaltenegger et al. 2007). In a modern Earth-like planet, there are very limited amounts of CO<sub>2</sub> due to natural processes that remove it from the atmosphere. For example, photosynthesis takes CO<sub>2</sub> out of the air and produces O<sub>2</sub> (as described in detail in Johnson (2016)); similarly, CO<sub>2</sub> is absorbed by chemical weathering - which transforms silicate rocks into carbonate rocks - and the weathering of carbonate minerals (Berner et al. 1983). Models of the Archean epoch suggest that CO<sub>2</sub> was much higher than now (Kaltenegger et al. 2007). Processes like these emphasize the need to study a wide range of CO<sub>2</sub> abundances. Determining the detectability strength of CO<sub>2</sub> given a variety of abundances will allow for a better understanding of the possibility of molecular detection on Earth-like planets with HWO.

In our study, we initially used modern-Earth abundances of H<sub>2</sub>O, CH<sub>4</sub>, and N<sub>2</sub>. We varied the abundance of CO<sub>2</sub> through five Earth-era abundances motivated by prior studies (Kaltenegger et al. 2007; Consortium\*† et al. 2023; Dr. Xin Lan & Dr. Ralph Keeling 2025). It is important to note that we tested two additional abundances that do not connect directly to Earth epochs to ensure a broad range of possible values without large leaps in abundance space, including a Venus-like abundance (Mahieux et al. 2023) and a ‘bridging’ abundance to examine the region in our abundance space between the Cenozoic and Proterozoic abundances. All CO<sub>2</sub> abundance values are shown in Table 3.

Additionally, due to the prominent overlapping spectral features of CO<sub>2</sub>, CH<sub>4</sub>, and H<sub>2</sub>O - which increases the difficulty in distinguishing the differences between molecules - we investigate the effect CO<sub>2</sub> has on the detectability of H<sub>2</sub>O and CH<sub>4</sub> and vice versa by testing a range of combined values. CO<sub>2</sub>-H<sub>2</sub>O test values are shown in the first and second columns of Table 4. CO<sub>2</sub>-CH<sub>4</sub> test values are shown in the first and third columns of Table 4.

We constrain our wavelength regime to wavelengths between 0.8-2.0 $\mu$ m, as there are no prominent CO<sub>2</sub> features at shorter wavelengths. Our grid is binned from a native resolving power of 500 to 70, following The LUVOIR Team

<sup>1</sup> <https://psg.gsfc.nasa.gov/apps/psgnest.php>

**Table 3.** Varying CO<sub>2</sub> abundances and their corresponding atmospheric archetypes

CO <sub>2</sub> Abundance (VMR)	Atmospheric Archetypes
$9.6 \times 10^{-1}$	Venus-like <sup>a</sup>
$1 \times 10^{-1}$	Archean <sup>b</sup>
$1 \times 10^{-2}$	Proterozoic <sup>b</sup>
$1 \times 10^{-3}$	Bridging
$3.65 \times 10^{-4}$	Paleozoic <sup>b</sup>
$7.2 \times 10^{-4}$	Cenozoic <sup>c</sup>
$4.2 \times 10^{-4}$	Modern <sup>d</sup>

<sup>a</sup> Mahieux et al. (2023)<sup>b</sup> Kaltenegger et al. (2007)<sup>c</sup> Consortium\*† et al. (2023)<sup>d</sup> Dr. Xin Lan & Dr. Ralph Keeling (2025)**Table 4.** Varying CO<sub>2</sub>, H<sub>2</sub>O, and CH<sub>4</sub> abundances used in the dual-detection simulations

CO <sub>2</sub> Abundance (VMR)	H <sub>2</sub> O Abundance (VMR)	CH <sub>4</sub> Abundance (VMR)
$9.6 \times 10^{-1}$	$1 \times 10^{-2}$	$7 \times 10^{-3}$
$1 \times 10^{-1}$	$3 \times 10^{-3}$	$3 \times 10^{-3}$
$1 \times 10^{-2}$	$1 \times 10^{-3}$	$1 \times 10^{-3}$
$1 \times 10^{-3}$	$3 \times 10^{-4}$	$3 \times 10^{-4}$
$7.2 \times 10^{-4}$	$1 \times 10^{-4}$	$1 \times 10^{-4}$

(2019) for NIR resolving power. For the simulations, we split the spectrum into 25 evenly spaced bandpasses of 20% widths to mimic a coronagraphic observation. We also vary the SNRs from 3-20 to understand at what SNRs different CO<sub>2</sub> abundances would be detectable.

## 2.2. KEN Grids

All BARBIE studies use grid-based retrievals. To ensure efficient production of new optimized spectral grids for grid-based retrievals, Himes et al. (in prep) developed the Python package, Gridder, which is a generalized grid-building scheme based on the methodology of Susemiel et al. (2023). Gridder produces arbitrary spectral grids using PSG. The Gridder parameter structure is very customizable, allowing any thermal profile and atmospheric chemistry in PSG to be used as a parameter in the grid.

Using Gridder, BARBIE3 (Latouf et al. 2025) developed and validated a new set of spectral grids called the KEN (no acronym - they're just KEN). These grids cover a larger wavelength range (0.2 - 2.0  $\mu$ m) at a native resolving power of R = 500, and have the same three base parameters: surface pressure (P<sub>0</sub>), surface albedo (A<sub>s</sub>), and gravity (g). KEN consists of four grids, each with a set of four different molecules, in addition to the three base parameters as seen in Table 5.

**Table 5.** KEN Grids

Grid Name	H <sub>2</sub> O	CO <sub>2</sub>	CO	O <sub>3</sub>	O <sub>2</sub>	CH <sub>4</sub>	SO <sub>2</sub>	N <sub>2</sub> O	N <sub>2</sub>
Merman Grid (M-KEN)	✓			✓	✓				✓
Beach Grid (B-KEN)	✓	✓				✓			✓
Allan Grid (A-KEN)				✓			✓	✓	✓
Lifeguard Grid (L-KEN)	✓	✓	✓						✓

When choosing a grid to use, we consider the molecule of interest and the relationship it has with other molecules. Thus, we used the L-KEN and B-KEN grids to investigate CO<sub>2</sub> and its relationships with CO (L-KEN), H<sub>2</sub>O (B-KEN), and CH<sub>4</sub> (B-KEN) in the NIR. For more information on the KEN grids and grid building, please refer to Latouf et al. (2025).

### 3. RESULTS

#### 3.1. $CO_2$ - $CO$ Detectability

We initially used L-KEN to study the detectability of  $CO_2$  and  $CO$  and found that with the highest  $CO$  abundance,  $1 \times 10^{-2}$  VMR, no strong  $CO$  detections are achievable. This is shown in Figure 3; with a SNR=20, only a weak detection is achievable between  $1.48$ - $1.71\mu m$ . Additionally, Figure 2 emphasizes the drastic difference in feature size between varying  $CO_2$  and  $CO$  features. Comparing spectral features of a Proterozoic-like  $CO_2$  abundance and the highest  $CO$  abundance - both  $1 \times 10^{-2}$  VMR - at  $1.58\mu m$ , the  $CO_2$  feature diminishes the apparent albedo by 0.3 whereas the  $CO$  feature diminishes the apparent albedo by 0.05. Since they are overlapping, the  $CO$  feature is overpowered by the larger  $CO_2$  feature, emphasizing the difficulty of strongly detecting  $CO$ . Due to this difference in spectral feature depth,  $CO$  would have an insignificant effect on the ability to detect  $CO_2$ . Therefore, for the rest of the study, we use B-KEN to study the impact of  $H_2O$  and  $CH_4$  on the detectability of  $CO_2$ , since these species have distinct and significant overlapping features in our wavelength range (shown in the bottom panel of Figure 1) and would more likely impact the detectability of  $CO_2$  at various abundances.

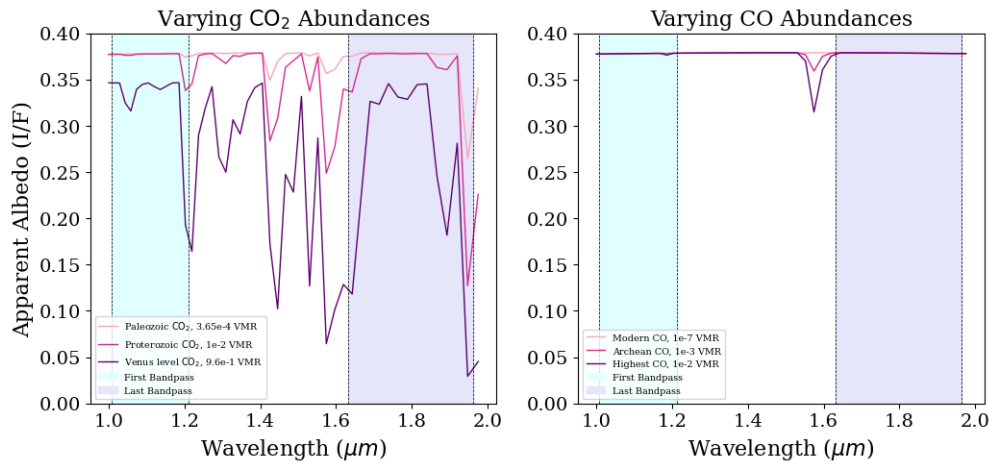


**Figure 2.**  $CO_2$  and  $CO$  spectral features at varying abundances from  $0.8$ - $2.0\mu m$ . It plots wavelength ( $\mu m$ ) on the x-axis and apparent albedo ( $I/F$ ) on the y-axis. We plot three  $CO_2$  abundances from Table 3: Paleozoic-like ( $3.65 \times 10^{-4}$  VMR) in light pink, Proterozoic-like ( $1 \times 10^{-2}$  VMR) in magenta, and a Venus-like ( $9.6 \times 10^{-1}$  VMR) in purple. We plot three  $CO$  abundances: Modern ( $1 \times 10^{-7}$  VMR - [Center for Science Education \(2017\)](#)) in light pink, Archean-like ( $1 \times 10^{-3}$  VMR - [Catling & Zahnle \(2020\)](#)) in magenta, and the highest abundance ( $1 \times 10^{-2}$  VMR - filler abundance) in purple. The first and last bandpasses are shaded in light blue and light purple, respectively.

#### 3.2. $CO_2$ Detectability with Modern $H_2O$ & $CH_4$ Abundances

In this section, we present our results for  $CO_2$  detectability with modern abundances of  $H_2O$  and  $CH_4$ . We note that Modern, Paleozoic-like, Cenozoic-like, and Bridging Earth  $CO_2$  abundances do not produce strong  $CO_2$  detections at any wavelength, abundance, or SNR with modern levels of  $CH_4$  and  $H_2O$ . Thus, our discussion will focus on the three highest  $CO_2$  abundances that produce strong  $CO_2$  detections at modern  $H_2O$  and  $CH_4$  abundances: Proterozoic-like, Archean-like, and Venus-like.

From Figure 2, we chose four bandpass centers -  $1.21\mu m$ ,  $1.44\mu m$ ,  $1.52\mu m$ , and  $1.63\mu m$  - that align with the deepest  $CO_2$  spectral features shortwards of  $1.95\mu m$ . At each bandpass center, we present the detectability strength of the four highest  $CO_2$  abundances as a function of SNR and abundance in Figure 4. The strength of detection is shown for each combination of  $CO_2$  abundance and SNR, where the darker the purple, the stronger the detection, and the lighter the pink, the more unconstrained the detection. Figure 4 provides clear insight into how wavelength, abundance, and SNR impact  $CO_2$  detectability.

In Figure 4a, at  $1.21\mu m$ , a Venus-like  $CO_2$  abundance is necessary to achieve a strong detection starting at SNR= 9. In Figure 4b, at  $1.44\mu m$ , a Venus-like  $CO_2$  abundance is required to achieve a strong detection at SNR= 14. In Figure 4c, at  $1.52\mu m$ , Venus-like, Archean-like, and Proterozoic-like  $CO_2$  abundances achieve strong detections starting at SNRs of 8, 9, and 15, respectively. In Figure 4d, at  $1.63\mu m$ , Venus-like, Archean-like, and Proterozoic-like  $CO_2$

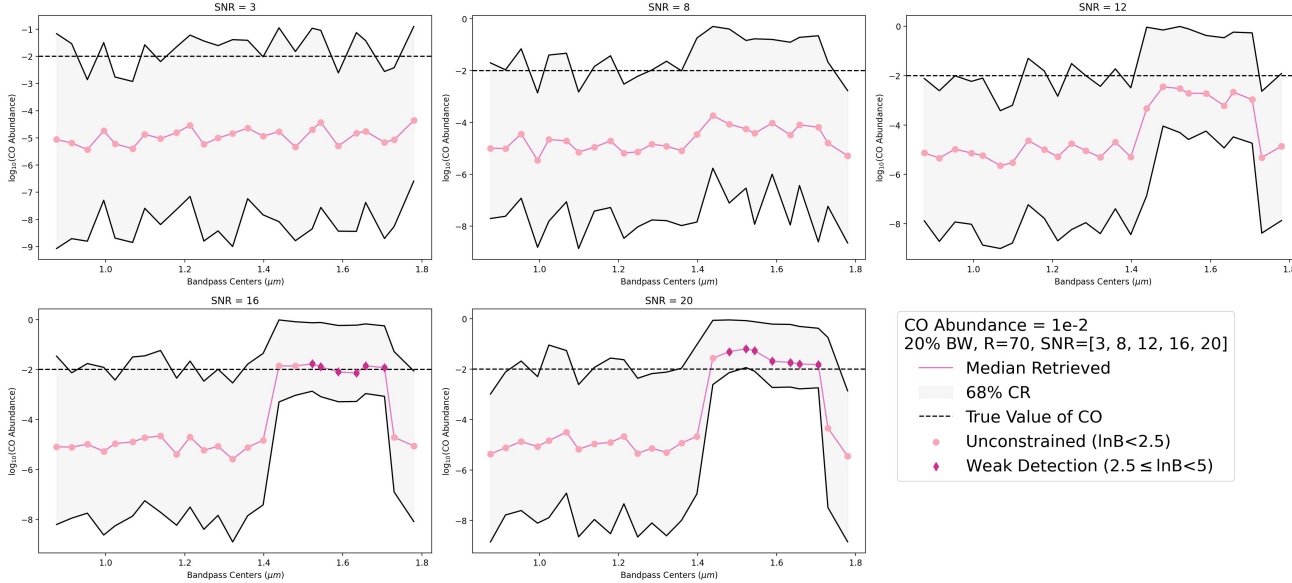


**Figure 3.** Strength of CO detections at SNRs of 3, 8, 12, 16 & 20 with the highest CO abundance,  $1 \times 10^{-2}$  VMR, throughout the wavelength range of 0.8-2.0 μm. Light pink circles portray unconstrained detections, magenta diamonds portray weak detections, and there are no strong detections. lnB classification follows the values in Table 2. The 68% credible region is shaded in grey. The true value of the CO abundance is marked by the horizontal dashed black line.

abundances achieve strong detections at SNRs of 6, 7, and 14, respectively. In Figures 4c and d, we notice a descending staircase pattern where, as we look to the right at increasing CO<sub>2</sub> abundances, the SNR required to achieve a strong detection is lower than the last. Furthermore, as seen in Figures 4a and b at 1.21 μm and 1.44 μm, strong detections are only achievable at a Venus-like CO<sub>2</sub> abundance compared to Figures 4c and d at 1.52 μm and 1.63 μm where Proterozoic-like and Archean-like CO<sub>2</sub> abundances are also able to achieve strong detections. Therefore, we confirm that longer wavelengths are necessary to achieve strong CO<sub>2</sub> detections for a wider range of CO<sub>2</sub> abundances - as low as  $1 \times 10^{-2}$  VMR.

As we consider the optimal long-wavelength cut-off for the HWO coronagraph, we want to be able to detect and characterize a wide range of CO<sub>2</sub> abundances that existed throughout Earth's history - not just a planetary archetype similar to Venus. Only in Figures 4c and d at 1.52 μm and 1.63 μm are we able to achieve strong CO<sub>2</sub> detections with CO<sub>2</sub> abundances lower than a Venus-like abundance. Thus, moving forward, it is essential to analyze the wavelength space between 1.52-1.63 μm in greater detail to ensure that we can study a variety of diverse worlds.

However, Figure 4a and b provide valuable insight on another essential topic of discussion - overlapping spectral features. Generally, we assume that deeper spectral features for a molecular species will naturally result in lower SNR requirements for detection - however, we see the opposite happening in Figure 4a and b. Looking at the left panel in Figure 2 where there are only spectral features coming from CO<sub>2</sub>, there is a deeper CO<sub>2</sub> feature at 1.44 μm compared to 1.21 μm. Despite this, we see in Figure 4a at 1.21 μm, a SNR=9 is required to achieve a strong CO<sub>2</sub> detection compared to Figure 4b at 1.44 μm, where a SNR=14 is required to achieve a strong CO<sub>2</sub> detection with a Venus-like CO<sub>2</sub> abundance. Thus, we see that a more shallow feature achieves a strong detection at a lower SNR; therefore, there must be an outside factor negatively impacting CO<sub>2</sub> detectability at 1.44 μm. As we zoom out and compare this to a modern-Earth spectrum where all molecular features are incorporated with a Venus-like CO<sub>2</sub> abundance in Figure 1, we see that at 1.44 μm there is a massive H<sub>2</sub>O feature overlapping with CO<sub>2</sub>, compared to 1.21 μm where CO<sub>2</sub> overlaps only with the tail end of a smaller H<sub>2</sub>O feature. This introduces the complexity of overlapping spectral features and how this effect impacts detectability, which we subsequently investigate at a deeper level.

Figure 5 summarizes Figure 4 by showing the minimum SNR required for a strong CO<sub>2</sub> detection at every bandpass center (μm) for the three strongly detectable CO<sub>2</sub> abundances. There are four things we can take away from this plot: (1) only at a Venus-like CO<sub>2</sub> abundance can we achieve a strong detection below 1.44 μm, (2) no detection is possible at 1.36 μm, which we can attribute to the presence of a massive H<sub>2</sub>O feature as seen in Figure 1, (3) the lowest and second-lowest SNRs required to achieve a strong CO<sub>2</sub> detection occur between 1.59-1.73 μm for all three

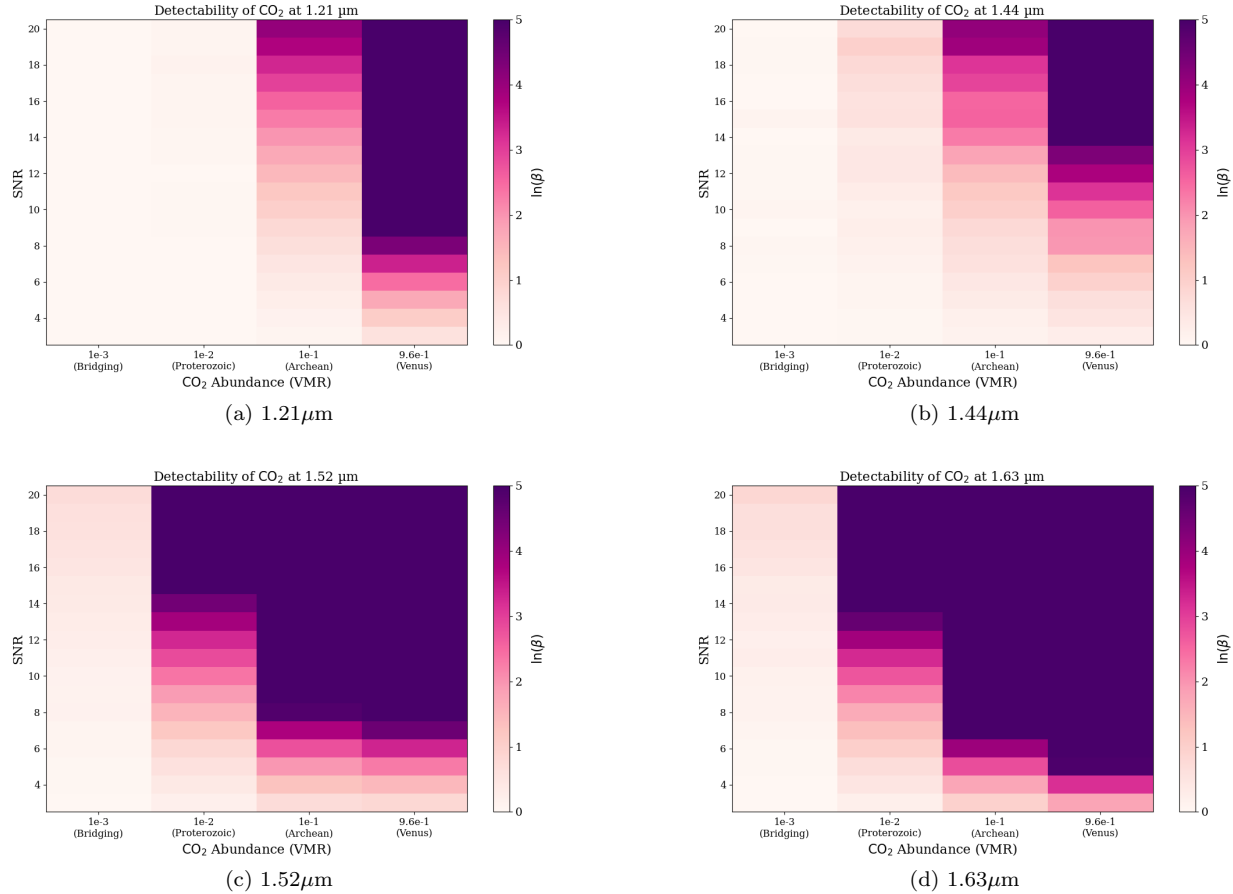


**Figure 4.** Strength of CO<sub>2</sub> detections at (a) 1.21  $\mu\text{m}$ , (b) 1.44  $\mu\text{m}$ , (c) 1.52  $\mu\text{m}$ , and (d) 1.63  $\mu\text{m}$  with respect to CO<sub>2</sub> abundance and SNR assuming a 20% bandpass. Columns on the x-axis are different CO<sub>2</sub> abundances; Bridging, Proterozoic-like, Archean-like, and Venus-like, from left to right. SNR values are on the y-axis. The strength of detection is shown for each combination of CO<sub>2</sub> abundance and SNR. As indicated by the color bar on the right side of each heat map, the darker the purple is, the stronger the detection is, and the lighter the pink is, the more unconstrained the detection is, following the same  $\ln(\beta)$  classifications defined in Table 2.

CO<sub>2</sub> abundances, and (4) at 1.78  $\mu\text{m}$ , we see an increase in SNR required to achieve a strong detection for all three CO<sub>2</sub> abundances.

Our first take away indicates that if we are characterizing a planet with a Venus-like CO<sub>2</sub> abundance with modern abundances of H<sub>2</sub>O and CH<sub>4</sub>, we would be able to strongly detect CO<sub>2</sub> at most wavelengths between 1.1-1.78  $\mu\text{m}$ . However, to characterize a planet with lower CO<sub>2</sub> abundances, we must look between 1.48-1.78  $\mu\text{m}$ . Our third and fourth points illustrate that to achieve a strong detection, the SNR requirements are lowest between 1.59-1.73  $\mu\text{m}$  and, in fact, increase after this point, meaning that it is unnecessary to consider going longer than a bandpass center of 1.73  $\mu\text{m}$  for the HWO long-wavelength cut-off. Additionally, just as we saw an irregularity at 1.44  $\mu\text{m}$  in Figure 4, we see another in Figure 5 at 1.36  $\mu\text{m}$  as stated in our second point - confirming that we need to investigate the impact of overlapping spectral features in greater detail.

To allow for a more in depth analysis, we create Figure 6 which shows the varying strength of detectability and the accuracy of the retrievals in greater detail from Proterozoic-like, Archean-like, and Venus-like CO<sub>2</sub> abundances, respectively. Not only does Figure 6 confirm our findings from Figure 4 and Figure 5 that shorter wavelengths and lower SNRs can be used at higher CO<sub>2</sub> abundances - it also shows us which specific wavelengths have detectability abnormalities such as a spike or drop. In Figure 6a, at a Proterozoic-like CO<sub>2</sub> abundance, the detectability plots look consistent with our previous conclusion that the number of strong detections increases at higher SNRs and at longer wavelengths without unexpected changes. However, we start to see some irregularities in Figure 6b which examines an

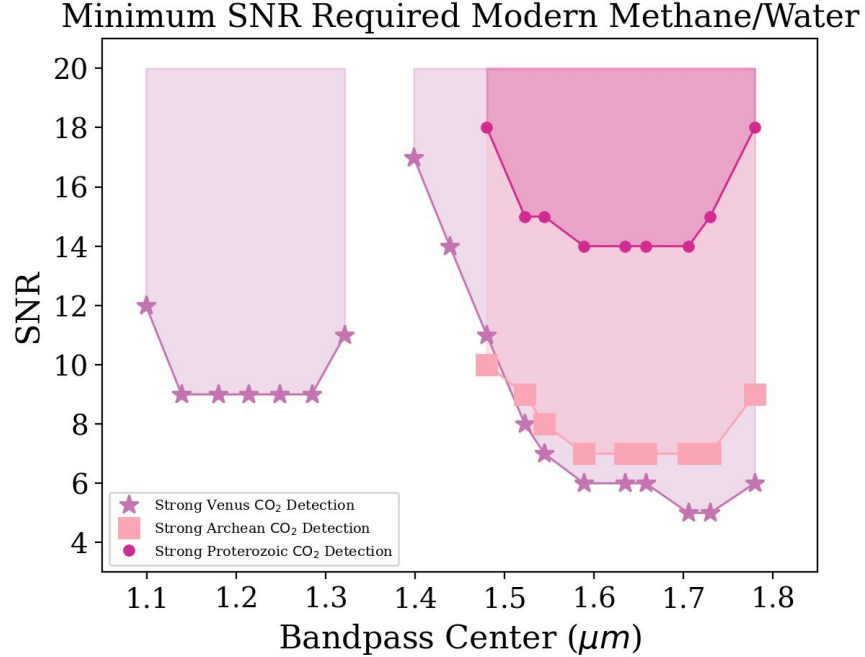


**Figure 5.** Minimum SNR required for a strong CO<sub>2</sub> detection at each bandpass center for the three highest CO<sub>2</sub> abundances that achieve strong detections. Venus-like is plotted in purple stars, Archean-like is plotted in light pink squares, and Proterozoic-like is plotted in magenta circles. The shaded regions represent the spaces in which you could achieve a strong detection for each abundance in their respective colors. The x-axis is bandpass center (μm) and the y-axis is SNR.

Archean-like abundance; we see a prominent dip in detectability strength at SNRs of 16 and 20 at 1.36 μm. Similarly, in Figure 6c which examines a Venus-like abundance, we see this dip in detectability at 1.36 μm at SNRs of 8, 12, 16 and 20. This tells us that something is affecting our ability to strongly detect CO<sub>2</sub> at 1.36 μm, just like we saw in Figure 5.

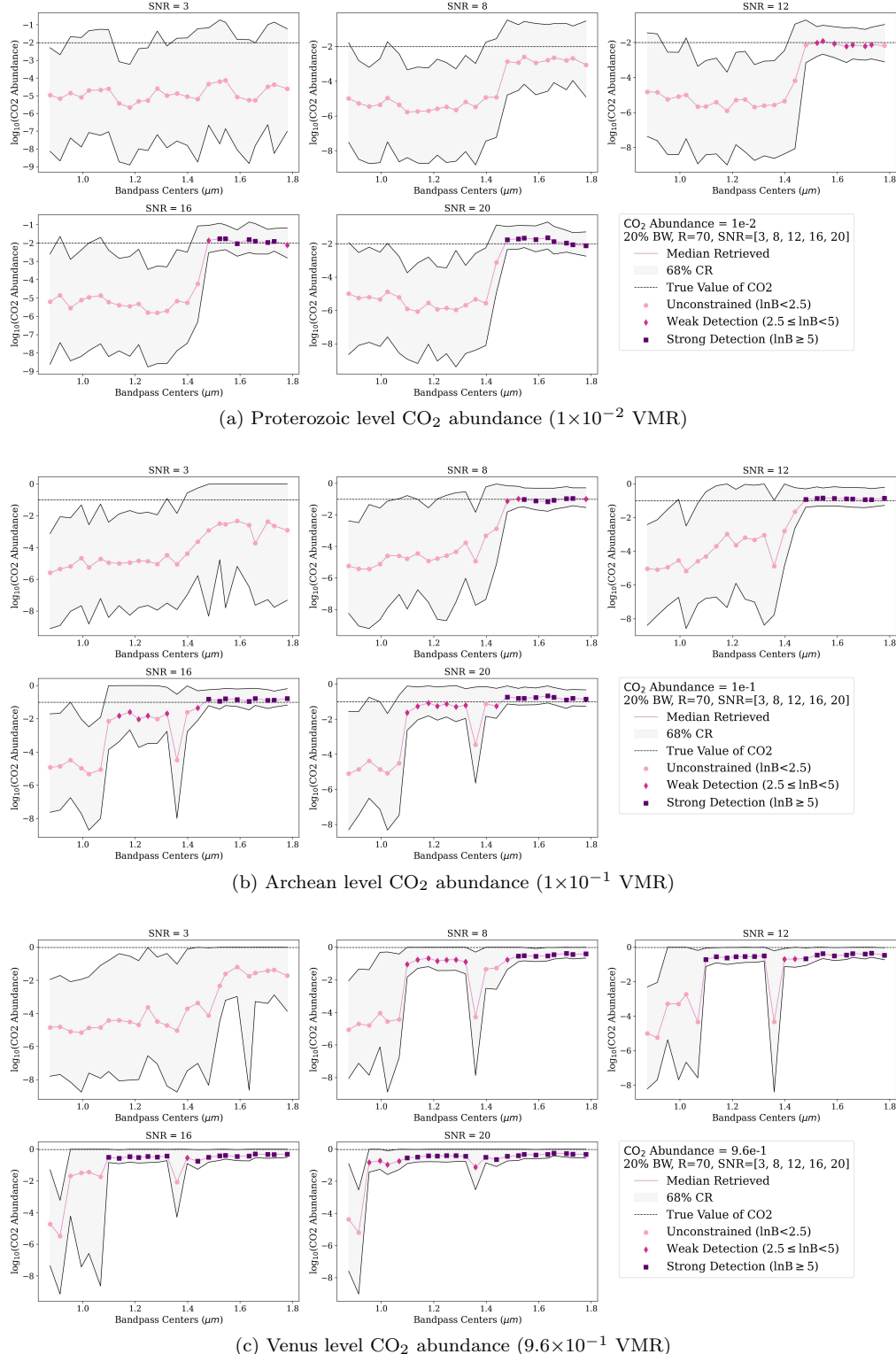
### 3.3. No H<sub>2</sub>O & Archean CH<sub>4</sub> Simulations

Due to the irregularities in Figure 4 at 1.44 μm in which a Venus-like abundance requires a higher SNR to be strongly detected compared to at 1.21 μm and Figure 5 and Figure 6 at 1.36 μm where we obtain a singularity of weakened CO<sub>2</sub> detections aligned with the massive H<sub>2</sub>O feature in the bottom panel of Figure 1, we hypothesize that the presence of H<sub>2</sub>O is negatively impacting the detectability of CO<sub>2</sub> even at the highest CO<sub>2</sub> abundance. This result led us to question which molecules and abundances could impact the detectability of CO<sub>2</sub>.

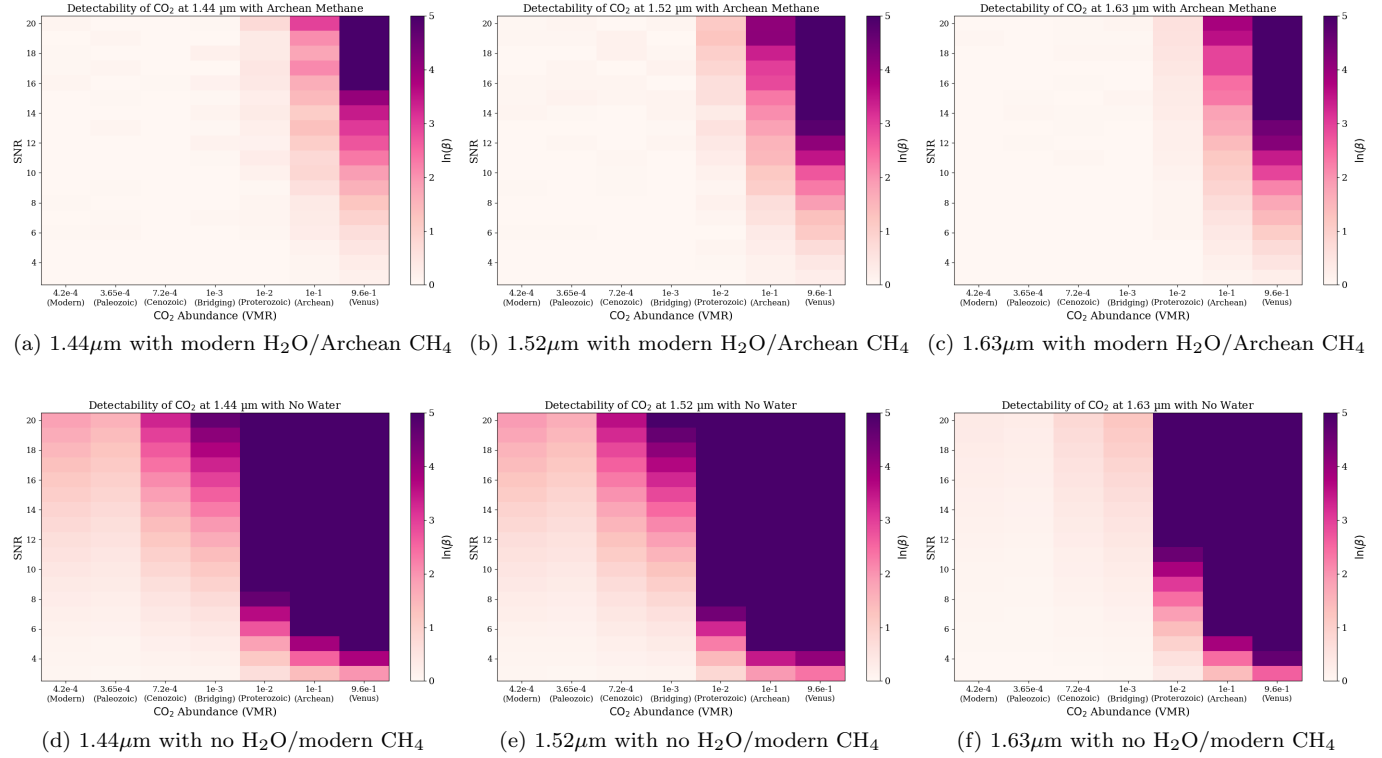
We simulated two additional tests that investigate how replacing (1) modern CH<sub>4</sub> with Archean CH<sub>4</sub> ( $7.07 \times 10^{-3}$ ), thereby increasing the CH<sub>4</sub> abundance, and (2) modern H<sub>2</sub>O with no H<sub>2</sub>O, thereby decreasing the H<sub>2</sub>O abundance, would change the detectability of CO<sub>2</sub>. Thus, Figure 7 allows for the analysis of the interconnected CO<sub>2</sub>, H<sub>2</sub>O, and CH<sub>4</sub> spectral features and the impact they have on the detectability of CO<sub>2</sub>.

Figure 7a at 1.44 μm, Figure 7b at 1.52 μm, and Figure 7c at 1.63 μm with modern H<sub>2</sub>O and Archean CH<sub>4</sub> show that with an increased abundance of CH<sub>4</sub>, the detectability of CO<sub>2</sub> decreases greatly across all abundances that had strong detections with modern CH<sub>4</sub>. For example, the minimum SNR for a strong detection increases from 14, 8, and 6 to 16, 14, and 14 for a Venus-like CO<sub>2</sub> abundance at 1.44 μm, 1.52 μm, and 1.63 μm, respectively. The opposite effect occurs when we set H<sub>2</sub>O to zero in Figure 7d at 1.44 μm, Figure 7e at 1.52 μm, and Figure 7f at 1.63 μm. Compared to the original modern H<sub>2</sub>O/CH<sub>4</sub> heat maps in Figure 4b (1.44 μm), c (1.52 μm), and d (1.63 μm), there is a dramatic increase in CO<sub>2</sub> detectability across the CO<sub>2</sub> abundances. For example, the minimum CO<sub>2</sub> abundance that achieves a strong CO<sub>2</sub> detection goes from CO<sub>2</sub> abundances of  $9.6 \times 10^{-1}$  VMR,  $1 \times 10^{-2}$  VMR, and  $1 \times 10^{-2}$  VMR to  $1 \times 10^{-2}$  VMR,  $1 \times 10^{-3}$  VMR, and  $1 \times 10^{-2}$  VMR for 1.44 μm, 1.52 μm, and 1.63 μm, respectively.

Due to the drastic impact that the presence of H<sub>2</sub>O and CH<sub>4</sub> have on the detectability of CO<sub>2</sub>, we simulated tests that vary the abundances of two different molecules at the same time. The simulations were done at 1.44 μm, 1.52 μm, and 1.63 μm, due to the strong overlapping features of CO<sub>2</sub> with CH<sub>4</sub>, H<sub>2</sub>O, or both as indicated in the bottom panel



**Figure 6.** Detectability strength of (a) Proterozoic-like, (b) Archean-like, and (c) Venus-like CO<sub>2</sub> abundances between 0.8–2.0 μm for a subset of SNRs, in this case 6, 10, 14, 18, and 20. The light pink circles portray an unconstrained detection, the magenta diamonds portray a weak detection, and the purple squares portray a strong detection which align with the lnB classifications defined in Table 2. The 68% credible region is shaded in grey. The true value of the CO<sub>2</sub> abundance is marked by the horizontal dashed black line.



**Figure 7.** Varying detection strength of CO<sub>2</sub> with respect to CO<sub>2</sub> abundance (on the x-axis) and SNR (on the y-axis) at bandpass centers of 1.44 $\mu\text{m}$  (a & d), 1.52 $\mu\text{m}$  (b & e), and 1.63 $\mu\text{m}$  (c & f). For each abundance and SNR, the color corresponds to the strength of the CO<sub>2</sub> detection; the darker the purple, the stronger the detection, and the lighter the pink, the more unconstrained the detection. The top plots (a, b, and c) show CO<sub>2</sub> detection strength for modern H<sub>2</sub>O and Archean CH<sub>4</sub>. The bottom plots (d, e, and f) show CO<sub>2</sub> detection strength for no H<sub>2</sub>O and modern CH<sub>4</sub>.

of Figure 1. We use the abundances of CH<sub>4</sub> and H<sub>2</sub>O from BARBIE3 which can be found in Table 4. It is important to note that we only ran CO<sub>2</sub>-H<sub>2</sub>O and CO<sub>2</sub>-CH<sub>4</sub> tests because BARBIE3 analyzes the relationship between H<sub>2</sub>O and CH<sub>4</sub>. Thus, BARBIE3 and this together give a comprehensive study of CO<sub>2</sub>, CH<sub>4</sub>, and H<sub>2</sub>O and the relationships between the three molecules in the NIR as functions of abundance, wavelength, and SNR.

### 3.4. CO<sub>2</sub>-CH<sub>4</sub> & CO<sub>2</sub>-H<sub>2</sub>O Simulations

Figure 8 and Figure 9 at 1.44 $\mu\text{m}$  (a), 1.52 $\mu\text{m}$  (b), and 1.63 $\mu\text{m}$  (c) illustrate the SNR required for a strong CO<sub>2</sub> detection. Figure 8 and Figure 9 at 1.44 $\mu\text{m}$  (d), 1.52 $\mu\text{m}$  (e), and 1.63 $\mu\text{m}$  (f) illustrate the SNR required for a strong CH<sub>4</sub> and H<sub>2</sub>O detection, respectively. The darker the purple, the higher the SNR, and the lighter the pink, the lower the SNR. These heat maps show how CO<sub>2</sub> and CH<sub>4</sub> (Figure 8) and CO<sub>2</sub> and H<sub>2</sub>O (Figure 9) affect the detectability of each other.

Figure 8a, b and c illustrate the SNR required to achieve a strong CO<sub>2</sub> detection at varying abundances of CO<sub>2</sub> and CH<sub>4</sub>. In Figure 8a at 1.44 $\mu\text{m}$ , high SNRs (14-17) are required for a strong CO<sub>2</sub> detection with a Venus-like CO<sub>2</sub> abundance at all CH<sub>4</sub> abundances. In Figure 8b at 1.52 $\mu\text{m}$ , low-high SNRs (9-16) are required for a strong CO<sub>2</sub> detection at a Venus-like CO<sub>2</sub> abundance across all CH<sub>4</sub> abundances and at an Archean-like CO<sub>2</sub> abundance at all except the highest CH<sub>4</sub> abundance. Similarly, in Figure 8c at 1.63 $\mu\text{m}$ , a strong CO<sub>2</sub> detection is achieved at mid-high SNRs (7-20) for Venus-like and Archean-like abundances of CO<sub>2</sub>. Additionally, a strong CO<sub>2</sub> detection is achievable at high SNRs (18-20) at a Proterozoic-like CO<sub>2</sub> abundance at the two lowest CH<sub>4</sub> abundances.

Figure 8d, e and f illustrate the SNR required to achieve a strong CH<sub>4</sub> detection at varying abundances of CO<sub>2</sub> and CH<sub>4</sub>. In Figure 8d at 1.44 $\mu\text{m}$ , the two highest CH<sub>4</sub> abundances require high SNRs (17-20) to strongly detect CH<sub>4</sub> at all CO<sub>2</sub> abundances except with a Venus-like CO<sub>2</sub> and second highest CH<sub>4</sub> abundance. In Figure 8e, we see a significant decrease in SNR requirements at 1.52 $\mu\text{m}$ : low-mid SNRs (4-13) achieve a strong CH<sub>4</sub> detection for the three highest CH<sub>4</sub> abundances at all CO<sub>2</sub> abundances, while medium SNRs are required for a CH<sub>4</sub> abundance of  $3 \times 10^{-4}$

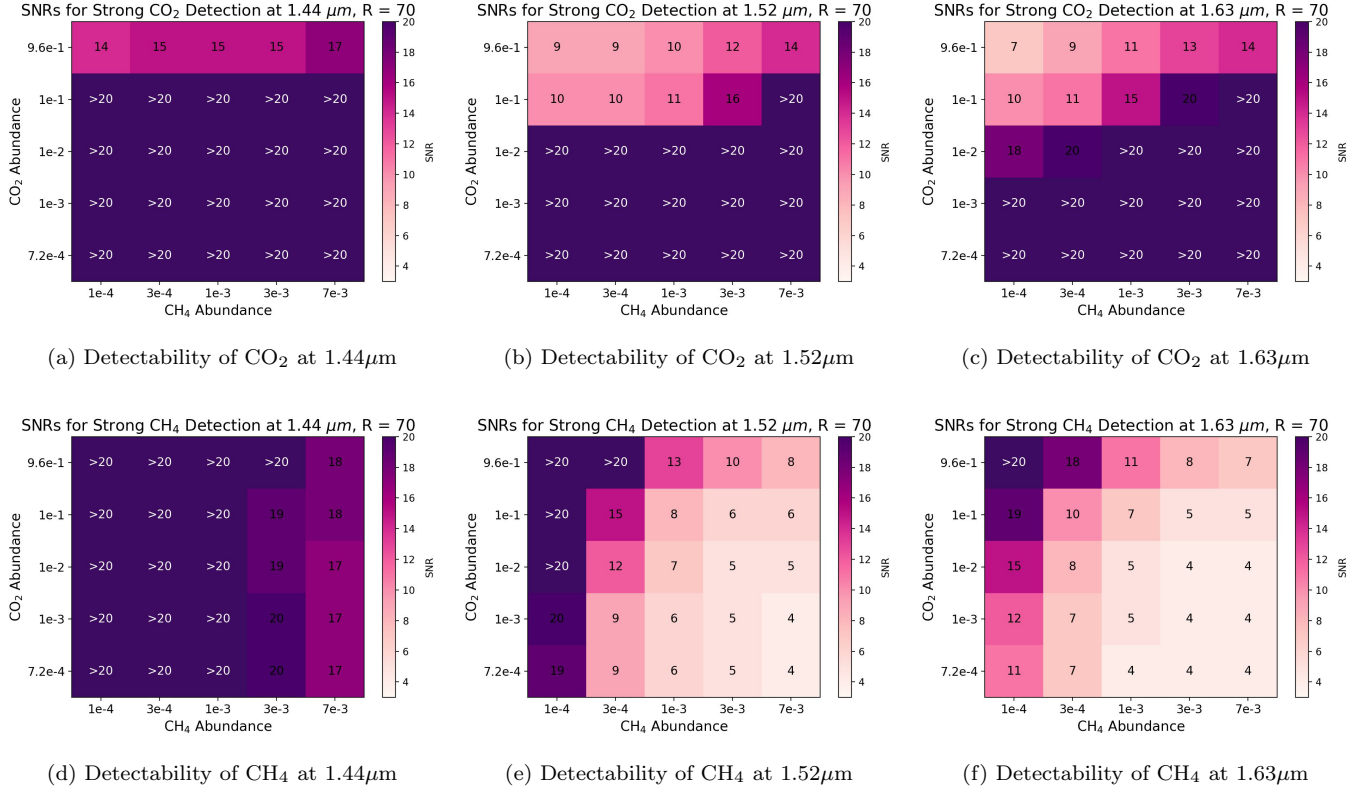


**Figure 8.** Top: Required SNR for a strong CO<sub>2</sub> detection at 1.44μm (a), 1.52μm (b), and 1.63μm (c). Bottom: Required SNR for a strong CH<sub>4</sub> detection at 1.44μm (d), 1.52μm (e), and 1.63μm (f). For each CO<sub>2</sub>-CH<sub>4</sub> combination, the necessary SNR required for a strong detection is shown, where darker colors correlate to higher SNRs and lighter colors correlate to lower SNRs. CH<sub>4</sub> abundances are plotted on the x-axis and CO<sub>2</sub> abundances are plotted on the y-axis. CH<sub>4</sub> and CO<sub>2</sub> abundances are taken from Table 4.

VMR with CO<sub>2</sub> abundances equal to or lower than  $1 \times 10^{-1}$  VMR, and high SNRs (19-20) are required for a strong CH<sub>4</sub> detection at the lowest CH<sub>4</sub> abundance and the two lowest CO<sub>2</sub> abundances. In Figure 8f at 1.63μm, low-mid SNRs (4-11) achieve a strong CH<sub>4</sub> detection equal to or lower than a CH<sub>4</sub> abundance of  $3 \times 10^{-4}$  VMR for all CO<sub>2</sub> abundances with the exception of the Venus-like CO<sub>2</sub> and  $3 \times 10^{-4}$  VMR CH<sub>4</sub> abundance which requires an SNR=18. Mid-high SNRs (11-19) achieve a strong CH<sub>4</sub> detection at the lowest CH<sub>4</sub> abundance for all except a Venus-like CO<sub>2</sub> abundance.

Figure 9a, b and c illustrate the SNR required to achieve a strong CO<sub>2</sub> detection at varying abundances of CO<sub>2</sub> and H<sub>2</sub>O. In Figure 9a at 1.44μm, mid-high SNRs (8-20) are required for a strong CO<sub>2</sub> detection at Venus-like, Archean-like, and Proterozoic-like CO<sub>2</sub> abundances. We see large increases in required SNR as the CO<sub>2</sub> and H<sub>2</sub>O abundances decrease. In Figure 9b at 1.52μm, strong CO<sub>2</sub> detections are achievable at low-mid SNRs (6-9) at Venus-like and Archean-like CO<sub>2</sub> abundances and mid-high SNRs (10-16) at a Proterozoic-like CO<sub>2</sub> abundance across all H<sub>2</sub>O abundances. In Figure 9c at 1.63μm, a strong CO<sub>2</sub> detection is achievable at low-mid SNRs (5-8) at Venus-like and Archean-like CO<sub>2</sub> abundances and mid-high SNRs (12-15) at a Proterozoic-like CO<sub>2</sub> abundance at all H<sub>2</sub>O abundances.

Figure 9d, e and f illustrate the SNR required to achieve a strong H<sub>2</sub>O detection at varying abundances of CO<sub>2</sub> and H<sub>2</sub>O. In Figure 9d at 1.44μm, mid-high SNRs (11-18) are required to achieve a strong H<sub>2</sub>O detection at all CO<sub>2</sub> and H<sub>2</sub>O abundances, except at a Venus-like CO<sub>2</sub> abundance and the two lowest H<sub>2</sub>O abundances which require SNRs> 20. In Figure 9e at 1.52μm, low-mid SNRs (4-13) are required to achieve a strong H<sub>2</sub>O detection for all H<sub>2</sub>O abundances across all CO<sub>2</sub> abundances except for a Venus-like CO<sub>2</sub> abundance combined with the lowest H<sub>2</sub>O abundance which requires an SNR>20 and the second lowest H<sub>2</sub>O abundance which requires an SNR=17. In Figure 9f at 1.63μm, low-mid SNRs (5-12) are required for the three highest H<sub>2</sub>O abundances at all CO<sub>2</sub> abundances to achieve a strong

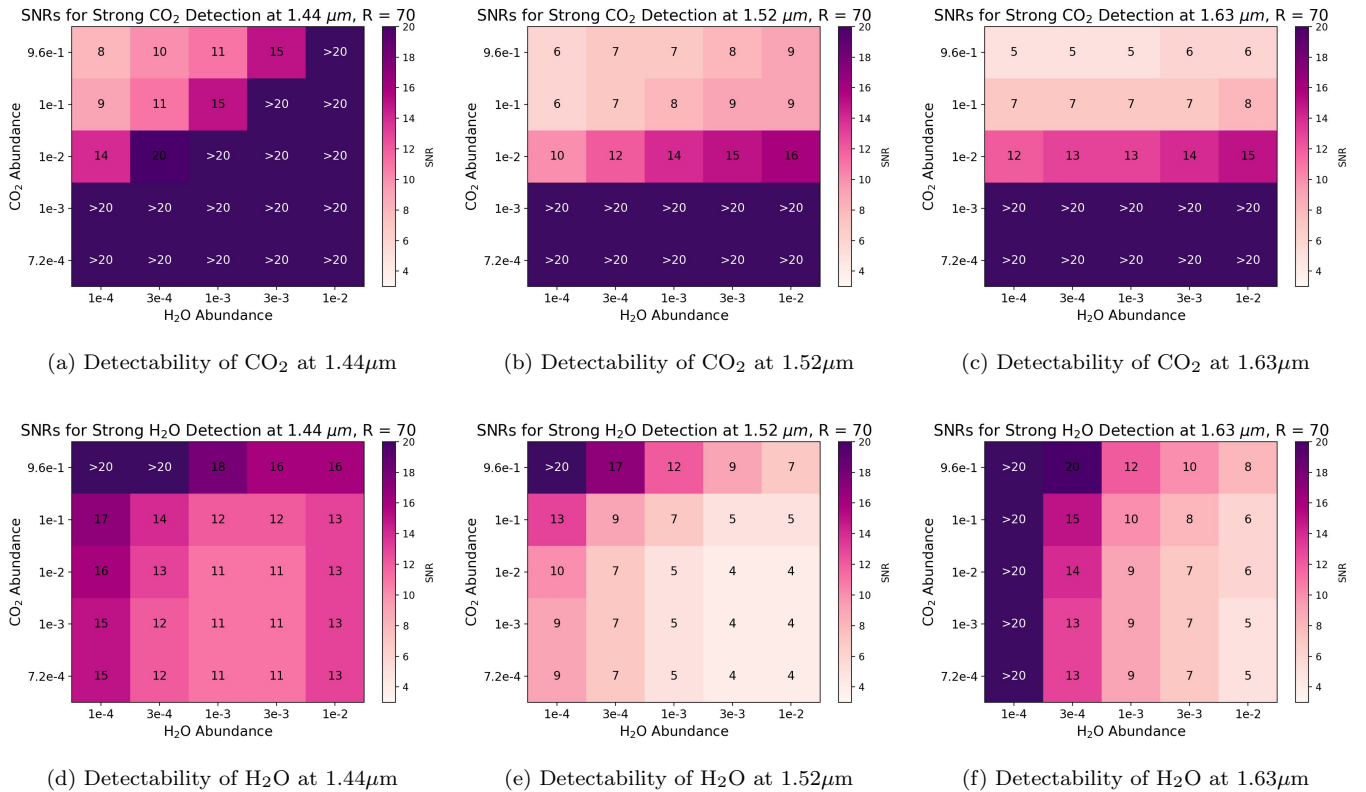


**Figure 9.** Top: Required SNR for a strong CO<sub>2</sub> detection at 1.44μm (a), 1.52μm (b), and 1.63μm (c). Bottom: Required SNR for a strong H<sub>2</sub>O detection at 1.44μm (d), 1.52μm (e), and 1.63μm (f). For each CO<sub>2</sub>-H<sub>2</sub>O combination, the necessary SNR required for a strong detection is shown, where darker colors correlate to higher SNRs and lighter colors correlate to lower SNRs. H<sub>2</sub>O abundances are plotted on the x-axis and CO<sub>2</sub> abundances are plotted on the y-axis. CH<sub>4</sub> and H<sub>2</sub>O abundances are taken from Table 4.

H<sub>2</sub>O detection. Mid-high SNRs (13-20) are required for a strong H<sub>2</sub>O detection at the second lowest H<sub>2</sub>O abundance at all CO<sub>2</sub> abundances. No strong H<sub>2</sub>O detections are achievable below an SNR of 20 at the lowest H<sub>2</sub>O abundance.

To optimize observing and characterizing rocky exoplanets with the HWO coronagraph, the goal is to be sensitive to the largest range of CO<sub>2</sub>, CH<sub>4</sub>, and H<sub>2</sub>O abundances as possible and to achieve strong CO<sub>2</sub> detections at the lowest SNRs. When looking at Figure 8 and Figure 9 as a whole, it is evident that bandpass centers of 1.52μm and 1.63μm achieve the most strong CO<sub>2</sub>, CH<sub>4</sub>, and H<sub>2</sub>O detections at the most diverse atmospheric compositions and the lowest SNRs. From previous BARBIE studies, we know that both H<sub>2</sub>O and CH<sub>4</sub> can be strongly detected at shorter wavelengths. Although it would be optimal to observe all three molecules at one wavelength, our main concern lies with the ability to strongly detect CO<sub>2</sub>. Thus, we can focus on Figure 8b and c and Figure 9b and c and analyze their differences.

The main difference between Figures 8b and c are the SNRs required to strongly detect CO<sub>2</sub> at an Archean-like and Proterozoic-like CO<sub>2</sub> abundance: Figure 8b at 1.52μm can achieve strong CO<sub>2</sub> detections at lower SNRs at an Archean-like CO<sub>2</sub> abundance. However, Figure 8c at 1.63μm, can achieve a strong CO<sub>2</sub> detection at a Proterozoic-like CO<sub>2</sub> abundance at the two lowest CH<sub>4</sub> abundances at very high SNRs (18-20).

Figures 9b and c are very similar; Figure 9c at 1.63μm requires a slightly lower SNR (1-3 difference) at every CO<sub>2</sub>-H<sub>2</sub>O combination to obtain a strong CO<sub>2</sub> detection compared to Figure 9b at 1.52μm.

However, we cannot make this decision by considering CO<sub>2</sub> detections alone. To determine a long-wavelength cut-off for the HWO coronagraph, we determined that there must be a balance between the detections we can achieve - pushing us to go to longer wavelengths - and the cost of cooling the telescope - pushing us to go to shorter wavelengths. Figures 8 and 9 reflect the detectability of CO<sub>2</sub> at bandpass centers of 1.52μm and 1.63μm. Thus, using a 20% bandpass width, a bandpass center of 1.52μm ranges from 1.396-1.679μm and a bandpass center of 1.63μm ranges from 1.499-1.803μm. Since the detections for both bandpasses are roughly equivalent, we find that a long-wavelength cut-off of 1.68μm

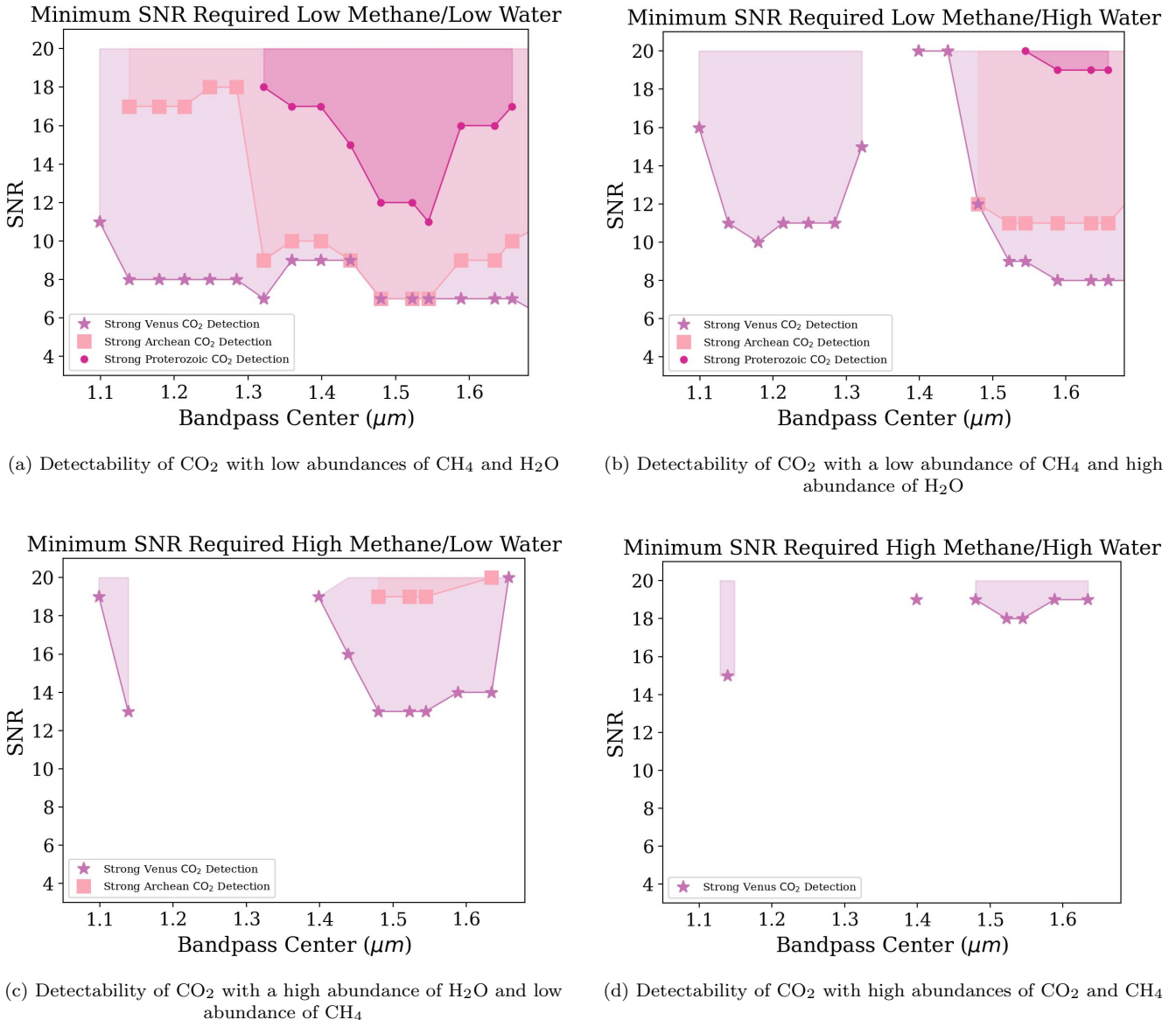


**Figure 10.** Minimum SNR required to achieve a strong CO<sub>2</sub> detection at each bandpass center for four varying planetary archetypes: (a) low CH<sub>4</sub> & low H<sub>2</sub>O, (b) low CH<sub>4</sub> & high H<sub>2</sub>O, (c) high CH<sub>4</sub> & low H<sub>2</sub>O, and (d) high CH<sub>4</sub> & high H<sub>2</sub>O. Bandpass center is plotted on the x-axis spanning 1.05-1.68 $\mu$ m and SNR is plotted on the y-axis. Varying abundances are plotted in different colors and shapes: Venus-like in light purple stars, Archean-like in light pink squares, and Proterozoic-like in dark pink circles. The relative shading corresponds to any area CO<sub>2</sub> is strongly detected and matches colors with the respective CO<sub>2</sub> abundance.

would be optimal in detecting CO<sub>2</sub> across various planetary archetypes and SNRs while requiring the least challenging telescope thermal requirements.

#### 3.4.1. Four Planetary Archetypes

With this optimal long-wavelength cut-off of 1.68 $\mu$ m for the HWO coronagraph, we can look at how different planetary archetypes would perform. Figure 10a, b, c & d show the minimum SNR required to achieve a strong CO<sub>2</sub> detection at varying combinations of CH<sub>4</sub> and H<sub>2</sub>O abundances: low/low, low/high, high/low & high/high. A low abundance of CH<sub>4</sub> and H<sub>2</sub>O are both  $1 \times 10^{-4}$  VMR and a high abundance of CH<sub>4</sub> and H<sub>2</sub>O are  $7 \times 10^{-4}$  VMR and  $1 \times 10^{-2}$  VMR, respectively. Strong CO<sub>2</sub> detections are plotted at varying CO<sub>2</sub> abundances: Venus-like in light purple

stars, Archean-like in light pink squares, and Proterozoic-like in dark pink circles. The shaded regions indicate areas of strong CO<sub>2</sub> detections for the respective CO<sub>2</sub> abundances.

Comparing the two extremes of low/low in Figure 10a and high/high in Figure 10d, we see that lower abundances of CH<sub>4</sub> and H<sub>2</sub>O result in more strong CO<sub>2</sub> detections across CO<sub>2</sub> abundance at lower SNRs. This confirms our hypothesis that entangled spectral features can cause degeneracy between molecules. This also informs us that we shouldn't prioritize a planetary archetype similar to Figure 10d which achieves strong detections only for a Venus-like CO<sub>2</sub> abundance at high SNRs over a shorter wavelength range compared to Figure 10a, b & c because we wouldn't be able to constrain the planet's atmospheric composition to great accuracy for varying levels of CO<sub>2</sub>.

Additionally, it is evident that high levels of methane negatively impact the detectability of CO<sub>2</sub> more significantly than a high H<sub>2</sub>O abundance. We know this because CO<sub>2</sub> achieves fewer strong detections in Figure 10c with high methane and low water compared to Figure 10d with high water and low methane. Thus, we must be vigilant particularly when looking at planetary archetypes with high levels of methane because although we may not achieve a strong CO<sub>2</sub> detection, it does not mean it is not present.

Figure 10 exemplifies how the complexity of overlapping and saturated features lead to spectral confusion, illustrating the intricacy of CO<sub>2</sub> detections. As spectral features saturate out, there are regions where there are no absorption. In addition to overlapping spectral features, this causes difficulties in differentiating molecules and their spectral features which could lead to confusion in which molecule it is strongly - or not strongly - detecting, impacting our results which is why we see some less intuitive points in our plots. For example, in Figure 10a, we see that Venus-like and Archean-like CO<sub>2</sub> abundances achieve strong CO<sub>2</sub> detections at the same SNRs between 1.48-1.54 $\mu$ m which is interesting considering the vast difference between their VMRs ( $9.6 \times 10^{-1}$  vs  $1 \times 10^{-1}$ ). However, if we look at the spectral features in this wavelength range, we are at the edge of a prominent CO<sub>2</sub> feature which could explain why it strongly detects vastly different CO<sub>2</sub> abundances at the same SNR. Comparing this to the middle of the CO<sub>2</sub> spectral feature between 1.59-1.63 $\mu$ m, Figure 10a shows that a Venus-like CO<sub>2</sub> abundance achieves strong CO<sub>2</sub> detections at lower SNRs compared to an Archean-like CO<sub>2</sub> abundance, which intuitively makes sense because a higher abundance correlates to stronger features. Thus, we must consider the spectral complexities when looking at plots like Figure 10.

In all four planetary archetypes, a Venus-like CO<sub>2</sub> abundance naturally achieves the most strong detections across our wavelength regime: as low as 1.1 $\mu$ m in Figures 10a, b and c and 1.14 $\mu$ m in Figure 10d. With this in mind, we conceive two different strategies for an initial survey of planetary properties: prioritizing looking for habitability with lower CO<sub>2</sub> abundances such as Archean-like or Proterozoic-like abundances at higher SNRs and longer wavelengths, or looking for uninhabitable atmospheres with ultra-high CO<sub>2</sub> abundances like a Venus-like abundance at shorter wavelengths and lower SNRs.

With current coronagraphic design conversations, having two parallel channels - one in the visible and one in the NIR - would allow us to confirm or rule out habitability in two ways: (1) observations in the visible, if present, could make a detection of water at wavelengths as short as 0.74 $\mu$ m (Latouf et al. 2023), suggesting habitable conditions, or (2) observations in the NIR, if present, could confirm the detection of a Venus-like CO<sub>2</sub> abundance as short as 1.1 $\mu$ m, suggesting uninhabitable conditions. By having parallel channels, we would not only be able to infer if a planet is habitable, but also have confirmation from the lack of a Venus-like CO<sub>2</sub> abundance.

However, in the case of non-parallel coronagraph channels, we argue that searching for both H<sub>2</sub>O and CH<sub>4</sub> in the visible should be the initial target for spectroscopy, due to their detectability and accessibility in the visible wavelength regime and their implications for life. Additionally, searching for CO<sub>2</sub> in the NIR would take longer than searching for H<sub>2</sub>O and CH<sub>4</sub> in the visible, meaning the priority for detecting CO<sub>2</sub> is secondary when parallel channels are not available.

#### 4. CONCLUSIONS

In this paper, we explored the conditions necessary to achieve a strong CO<sub>2</sub> detection based on molecular abundance, SNR, and wavelength using the BARBIE methodology and KEN grid set. Using L-KEN, we found that at modern levels of CO, there is an insignificant impact on the detectability of CO<sub>2</sub> and no strong CO detections are achievable at the highest CO abundance. Using B-KEN, we found that with modern levels of H<sub>2</sub>O and CH<sub>4</sub>, only the three highest CO<sub>2</sub> abundances in our test - Venus-like, Archean-like, and Proterozoic-like - result in strong CO<sub>2</sub> detections. We found strong links between SNR, abundance, and wavelength for the case of CO<sub>2</sub>. Generally, stronger detections are more likely at higher SNRs and longer wavelengths. We also found that with increasing abundance, there are more strong detections at lower SNRs and shorter wavelengths. This study also described the detectability relationships

of CO<sub>2</sub>-H<sub>2</sub>O and CO<sub>2</sub>-CH<sub>4</sub>. We confirm that there is a strong correlation between these molecules and their impact on detectability of each other at NIR wavelengths. In particular, greater abundances of H<sub>2</sub>O and CH<sub>4</sub> increased the difficulty to detect CO<sub>2</sub>.

Each of our results allow us to better constrain the optimal long-wavelength cut-off for the HWO coronagraph and understand the inter-connectedness between CO<sub>2</sub>, H<sub>2</sub>O, and CH<sub>4</sub>. Figure 1, showing thermal noise due to the blackbody emission of the telescope as a function of telescope temperature and wavelength (top) and CO<sub>2</sub>, CH<sub>4</sub>, H<sub>2</sub>O, CO, and O<sub>2</sub> spectral features between 0.8-2.0 $\mu$ m (bottom), illustrates that longer wavelengths would drastically increase the cost from cooling the telescope due to the increase in noise as the telescope warms and emphasizes the rationale for studying CO<sub>2</sub> due its prominent features at longer wavelengths - specifically looking at the feature that peaks at 1.6 $\mu$ m. Figure 4 showed us that analyzing the wavelength regime between the bandpass centers of 1.52-1.63 $\mu$ m would result in the maximum number of strong detections across CO<sub>2</sub> abundance and SNR. Figure 5 showed us that Venus-like, Archean-like, and Proterozoic-like CO<sub>2</sub> abundances can be strongly detected at their respective lowest SNRs starting at 1.59 $\mu$ m and proved that it is unnecessary to go longer than 1.7 $\mu$ m because it does not provide additional valuable information. Figure 6 emphasized that there are outside factors besides CO<sub>2</sub> abundance and SNR that could impact CO<sub>2</sub> detectability which led us to simulate tests varying CH<sub>4</sub> and H<sub>2</sub>O abundances. Figure 7 confirmed that an increased abundance of CH<sub>4</sub> resulted in less strong CO<sub>2</sub> detections and a decreased abundance of H<sub>2</sub>O resulted in more strong CO<sub>2</sub> detections. Because of this, we tested a variety of different CH<sub>4</sub> and H<sub>2</sub>O abundances as seen in Figure 8 and Figure 9, respectively. These plots demonstrated that 1.52 $\mu$ m was the optimal bandpass center that provided the most strong CO<sub>2</sub> detections across all abundances with the lowest SNRs and reasonable cost. In addition, although CH<sub>4</sub> and H<sub>2</sub>O can be strongly detected at shorter wavelengths, as seen in previous BARBIE studies, 1.52 $\mu$ m also provided optimal CH<sub>4</sub> and H<sub>2</sub>O detections. Figure 10 showing CO<sub>2</sub> detectability at various planetary archetypes emphasized that lower abundances of CH<sub>4</sub> and H<sub>2</sub>O positively impact our ability to strongly detect CO<sub>2</sub>. In addition, it confirmed that a long-wavelength cut-off of 1.68 $\mu$ m - with a bandpass center of 1.52 $\mu$ m - is optimal for strongly detecting various abundances of CO<sub>2</sub>. However, detecting a Venus-like CO<sub>2</sub> abundance as low as 1.1 $\mu$ m could allow us to rule out a habitable atmosphere if present.

By combining all of our results, we conclude that the optimal bandpass center to strongly observe CO<sub>2</sub> is 1.52 $\mu$ m, meaning that 1.68 $\mu$ m is the optimal long-wavelength cut-off for the HWO coronagraph to be able to sufficiently achieve strong CO<sub>2</sub> detections at varying CO<sub>2</sub>, H<sub>2</sub>O, and CH<sub>4</sub> abundances at the lowest SNRs.

The next steps in the BARBIE world are to explore the molecular detection requirements in the UV using the KEN grid set, which will help dictate the technological requirements of HWO in the UV. With the KEN grids, our studies focus on a specific set of biosignatures. We encourage others to study the detectability of other potential biosignatures such as methyl halides (CH<sub>3</sub>Cl, CH<sub>3</sub>Br, and CH<sub>3</sub>I), dimethyl sulfide (DMS), and dimethyl disulfide (DMDS) to confirm whether a 1.68 $\mu$ m cut-off for the HWO coronagraph will be sufficient for strongly detecting these molecules as well.

#### ACKNOWLEDGMENTS

C. H. acknowledges the financial support from SURA and CRESST II. She acknowledges Dr. Avi Mandell and Dr. Natasha Latouf for their support and guidance as they brought her onto the BARBIE team. She also gratefully acknowledges Greta Gerwig, Margot Robbie, Ryan Gosling, Emma Mackey, and Mattel Inc.<sup>TM</sup> for Barbie (doll, movie, and concept), for which this project is named after. N. L. gratefully acknowledges financial support from a NASA FINESST and an appointment to the NASA Postdoctoral Program (NPP) at the NASA Goddard Space Flight Center, administered by Oak Ridge Associated Universities under contract with NASA. The material is based upon work supported by NASA under award number 80GSFC24M0006. The authors would like to thank the Sellers Exoplanet Environments Collaboration (SEEC) and ExoSpec teams at NASA's Goddard Space Flight Center for their consistent support. These Barbies are astrophysicists!

#### REFERENCES

Akeson, R. L., Chen, X., Ciardi, D., et al. 2013, PASP, 125, 989, doi: [10.1086/672273](https://doi.org/10.1086/672273)

Benneke, B., & Seager, S. 2013, ApJ, 778, 153, doi: [10.1088/0004-637X/778/2/153](https://doi.org/10.1088/0004-637X/778/2/153)

Berner, R. A., Lasaga, A. C., & Garrels, R. M. 1983, Am. J. Sci.; (United States), 283:7, doi: [10.2475/ajs.283.7.641](https://doi.org/10.2475/ajs.283.7.641)

Catling, D. C., & Zahnle, K. J. 2020, Science Advances, 6, eaax1420, doi: [10.1126/sciadv.aax1420](https://doi.org/10.1126/sciadv.aax1420)

Center for Science Education. 2017

Consortium\*†, T. C. C. P. I. P. C., Hönnisch, B., Royer, D. L., et al. 2023, *Science*, 382, eadi5177, doi: [10.1126/science.ad5177](https://doi.org/10.1126/science.ad5177)

Dr. Xin Lan, N. g., & Dr. Ralph Keeling, S. I. o. O. s. 2025. <https://gml.noaa.gov/ccgg/trends/>

Feinberg, L. 2016, LUVOIR Tech Note Series

Feng, Y. K., Robinson, T. D., Fortney, J. J., et al. 2018, *AJ*, 155, 200, doi: [10.3847/1538-3881/aab95c](https://doi.org/10.3847/1538-3881/aab95c)

Gaudi, B. S., Seager, S., Mennesson, B., et al. 2020, arXiv e-prints, arXiv:2001.06683, doi: [10.48550/arXiv.2001.06683](https://doi.org/10.48550/arXiv.2001.06683)

Gordon, I., Rothman, L., Hargreaves, R., et al. 2022, *Journal of Quantitative Spectroscopy and Radiative Transfer*, 277, 107949, doi: <https://doi.org/10.1016/j.jqsrt.2021.107949>

Harrington, J., Himes, M. D., Cubillos, P. E., et al. 2022, *PSJ*, 3, 80, doi: [10.3847/PSJ/ac3513](https://doi.org/10.3847/PSJ/ac3513)

Himes, M. D., Mandell, A. M., Latouf, N., & Villanueva, G. L. in prep

Johnson, M. P. 2016, *Essays in Biochemistry*, 60, 255, doi: [10.1042/EBC20160016](https://doi.org/10.1042/EBC20160016)

Juanola-Parramon, R., Zimmerman, N. T., Pueyo, L., et al. 2022, *Journal of Astronomical Telescopes, Instruments, and Systems*, 8, 034001, doi: [10.11117/1.JATIS.8.3.034001](https://doi.org/10.11117/1.JATIS.8.3.034001)

Kaltenegger, L., Traub, W. A., & Jucks, K. W. 2007, *ApJ*, 658, 598, doi: [10.1086/510996](https://doi.org/10.1086/510996)

Latouf, N., Himes, M. D., Mandell, A. M., et al. 2025, *AJ*, 169, 50, doi: [10.3847/1538-3881/ad9729](https://doi.org/10.3847/1538-3881/ad9729)

Latouf, N., Mandell, A. M., Villanueva, G. L., et al. 2023, *AJ*, 166, 129, doi: [10.3847/1538-3881/acebc3](https://doi.org/10.3847/1538-3881/acebc3)

—. 2024, *AJ*, 167, 27, doi: [10.3847/1538-3881/ad0fde](https://doi.org/10.3847/1538-3881/ad0fde)

Mahieux, A., Robert, S., Piccialli, A., Trompet, L., & Vandaele, A. 2023, *Icarus*, 405, 115713, doi: <https://doi.org/10.1016/j.icarus.2023.115713>

Mayor, M., & Queloz, D. 1995, *Nature*, 378, 355, doi: [10.1038/378355a0](https://doi.org/10.1038/378355a0)

National Academies of Sciences, Engineering, and Medicine. 2021, *Pathways to Discovery in Astronomy and Astrophysics for the 2020s*, doi: [10.17226/26141](https://doi.org/10.17226/26141)

Roberge, A., & Moustakas, L. A. 2018, *Nature Astronomy*, 2, 605, doi: [10.1038/s41550-018-0543-8](https://doi.org/10.1038/s41550-018-0543-8)

Susemehl, N., Mandell, A. M., Villanueva, G. L., et al. 2023, *AJ*, 166, 86, doi: [10.3847/1538-3881/ace43b](https://doi.org/10.3847/1538-3881/ace43b)

The LUVOIR Team. 2019, arXiv e-prints, arXiv:1912.06219. <https://arxiv.org/abs/1912.06219>

Villanueva, G., Smith, M., Protopapa, S., Faggi, S., & Mandell, A. 2018, *Journal of Quantitative Spectroscopy and Radiative Transfer*, 217, 86–104, doi: [10.1016/j.jqsrt.2018.05.023](https://doi.org/10.1016/j.jqsrt.2018.05.023)